Growth of InAs/InAsSb heterostructured nanowires

Growth of InAs/InAsSb heterostructured nanowires

Daniele Ercolani[1], Mauro Gemmi[2], Lucia Nasi[3], Francesca Rossi[3], Marialilia Pea[1], Ang Li[1], Giancarlo Salviati[3], Fabio Beltram[1] and Lucia Sorba[1]

[1] NEST, Scuola Normale Superiore and Istituto Nanoscienze—CNR, Pisa, Italy
[2] Center for Nanotechnology Innovation @ NEST, Istituto Italiano di Tecnologia, Pisa, Italy
[3] CNR-IMEM, Parma, Italy

E-mail: daniele.ercolani@sns.it

Abstract

We report the growth of InAs/InAs$_{1-x}$Sb$_x$ single and double heterostructured nanowires by Au-assisted chemical beam epitaxy. The InAs$_{1-x}$Sb$_x$ nanowire segments have been characterized in a wide range of antimony compositions. Significant lateral growth is observed at intermediate compositions ($x \sim 0.5$), and the nucleation and step-flow mechanism leading to this lateral growth has been identified and described. Additionally, CuPt ordering of the alloy has been observed with high resolution transmission electron microscopy, and it is correlated to the lateral growth process. We also show that it is possible to regrow InAs above the InAsSb alloy segment, at least up to an intermediate antimony composition. Such double heterostructures might find applications both as mid-infrared detectors and as building blocks of electronic devices taking advantage of the outstanding electronic and thermal properties of antimonide compound semiconductors.

S Online supplementary data available from stacks.iop.org/Nano/23/115606/mmedia

(Some figures may appear in colour only in the online journal)

1. Introduction

Mid-infrared detectors are currently based on HgCdTe alloys. However, the synthesis of such alloys poses non-trivial health and environmental hazards together with the problem of handling the liquid waste of Hg in growth chambers and reactors. InAsSb alloys are attractive substitutes, having a tunable bandgap covering most of the mid-infrared spectrum (2–8 μm) and being composed of much safer and easier to handle constituents. The large lattice mismatch of InAsSb with the available substrates has so far hindered its development due to strain-induced defects and the consequent degradation of material quality. In nanowires (NWs) interfacial strain does not induce crystal defects even in the extreme case of InAs/InSb heterostructured NWs [1, 2], since the strain is easily relaxed at the free surface. Furthermore, antimonide materials are currently emerging as important compounds due to their very high bulk electron and hole mobility. In particular, InSb has the smallest band gap,

the smallest effective mass, and the largest Landé g-factor. These make InSb and InAsSb alloys ideal candidates for high speed devices [3] and spin-related applications [4]. InAs, on the other hand, is an outstanding material for devices due to its intrinsic high conductivity and the easiness of fabrication of Ohmic and high transparency contacts [5]. In addition, InAs/InAs$_{1-x}$Sb$_x$ heterostructures—for a wide x compositional range—have a very interesting broken gap, type II band alignment [6] which, along with the absence of strain-related defects typical of NWs, allows an unprecedented flexibility in band engineering [7]. Apart from an in-depth x-ray diffraction study on MOVPE grown InAsSb NWs [8] and a very recent work on InAsSb NW surfaces [28], reports on antimonide–arsenide alloy NWs have rather focused on the GaAs/GaAsSb system [9, 10].

It appears that the growth of arsenide segments above antimonide NWs presents great challenges, hindering the fabrication of double heterostructures, antimonide-based quantum dots, and in general reducing the degrees of freedom

Table 1. Growth conditions and measured parameters of InAs$_{1-x}$Sb$_x$ segments. Data for InSb is taken from [1].

Sample	P_{TDMASb} (Torr)	P_{TBAs} (Torr)	R	x	Lateral growth (nm min^{-1})	Catalyst at.%	
						In	Au
A	0.10	1.00	0.11	<0.10	~0.13	33	67
B	0.37	0.50	0.48	0.12	0.22 ± 0.07	33	67
C	0.75	0.50	0.65	0.25	~0.5	34	64
D	0.75	0.30	0.75	0.50	0.58 ± 0.10	33	67
E	0.75	0.10	0.90	0.70	0	44	51
InSb	0.75	0	1.00	0.94	0	67	33

in device design. In this work we show the growth of complex InAs/InAs$_{1-x}$Sb$_x$/InAs heterostructured nanowires, at least up to an intermediate Sb content, and we present results on the growth dynamics of InAs$_{1-x}$Sb$_x$ alloys in a wide compositional range on InAs stems. Particular attention is devoted to the unusual lateral growth mechanism which is explained with a nucleation and step-flow model.

2. Experimental details

Axial InAs/InAs$_{1-x}$Sb$_x$ single and double heterostructured NWs have been grown on InAs(111)B substrates by chemical beam epitaxy (CBE) in a Riber Compact-21 System, by Au-assisted growth [11]. The system employs pressure control of the metalorganic (MO) precursors in the lines to vary the precursor flux on the sample during growth. The precursors used for the NW growth are trimethylindium (TMIn), tertiarybutylarsine (TBAs), and tert-dimethylaminoantimony (TDMASb). TDMASb was chosen as Sb precursor over the more commonly used trimethylantimony (TMSb) for its lower decomposition temperature, which gives a large advantage in terms of the growth temperature window. Precursor flux into the growth chamber is proportional to the corresponding line pressure. Details on how the fluxes are compared can be found in the supporting information (available at stacks.iop. org/Nano/23/115606/mmedia).

Au nanoparticles have been realized by thermal dewetting of nominally 0.5 nm thick gold films. The gold has been deposited by thermal evaporation on InAs wafers in a separate evaporator chamber and then transferred into the CBE system. In the CBE chamber, the samples have been heated under TBAs flow for 20 min at $500 \pm 5\,^{\circ}$C in order to remove the surface oxide and to dewet the Au film into nanoparticles. The resulting nanoparticles have a wide diameter range with an average size of the order of 50 nm.

The InAs segments have been grown for 60 or 75 min at a temperature of $420 \pm 5\,^{\circ}$C, with MO line pressures of 0.3 and 1.0 Torr for TMIn and TBAs, respectively. Then, to grow the InAs$_{1-x}$Sb$_x$ segments, the TMIn line pressure has been abruptly changed to 0.45 Torr while TBAs and TDMASb fluxes were set to the values reported in table 1, with no change in growth temperature. InAs$_{1-x}$Sb$_x$ growth has proceeded for another 60 min for most of the NW samples. At the end of the growth the TMIn flux has been stopped and the sample cooled down under TDMASb and TBAs flow. For InAs/InAs$_{1-x}$Sb$_x$/InAs double heterostructures, the

growth has been concluded after additional 30 min of InAs grown in the same conditions as the first segment, with growth termination under TBAs flow. NWs have been characterized by scanning electron microscopy (SEM) with an accelerating voltage of 3–8 kV in a Zeiss Ultraplus Field Emission SEM, with the substrate tilted by 45° or 60°. Additionally, for most samples, the NWs have been mechanically transferred on carbon coated copper grids by gently rubbing the grids on the substrate, and analyzed by means of high resolution transmission electron microscopy (HRTEM) and energy dispersive x-ray spectroscopy (EDX) in a JEOL 2200FS microscope working at 200 keV, and by transmission electron microscopy (TEM) and electron diffraction measurements in a Zeiss Libra 120 microscope working at 120 keV. The composition by EDX was estimated by the standardless ratio method, considering the characteristic L lines of In, As, and Sb.

3. Results

InAs/InAs$_{1-x}$Sb$_x$/InAs double heterostructured nanowires have been grown in a wide range of TDMASb and TBAs flux ratios to investigate the possibility of InAs regrowth after an antimonide section. We indicate with R the Sb fraction of the total (effective) group V flow in the chamber. If we call F_{TDMASb} (F_{TBAs}) the TDMASb (TBAs) flux (in # of moles entering the growth chamber per unit time) then R is equal to $R = F_{\text{TDMASb}}/(F_{\text{TDMASb}} + F_{\text{TBAs}})$. As detailed in the supporting information (available at stacks.iop.org/Nano/23/115606/mmedia), F_{TBAs} is also corrected for cracking at the injector, resulting in the effective flow of 'incorporable' arsenic. Figure 1 shows a series of InAs/InAs$_{1-x}$Sb$_x$/InAs double heterostructured NW samples with varying TDMASb flux fraction R; the Sb precursor flux is increasing from $R = 0.31$ (figure 1(a)) up to $R = 0.82$ (figure 1(f)). All the images are taken with a tilt angle of 45° (except figure 1(a) which is taken at grazing incidence). Figures 1(b)–(f) share the same scale bar. The InAs base, grown for 75 min, is straight and apparently without defects. The alloy segment, grown for 10 min, is distinguishable for its increased diameter and different faceting (see figures 1(a)–(e)), which will be described later. The top InAs part is grown for 30 min and is clearly identifiable for its smaller diameter and the presence of the catalyst particle at the tip. Figures 1(g) and (h) are TEM micrographs of a NW of the sample depicted in figure 1(d), with $R = 0.70$. In the bright field image (figure 1(g)) it is easy to identify the main features
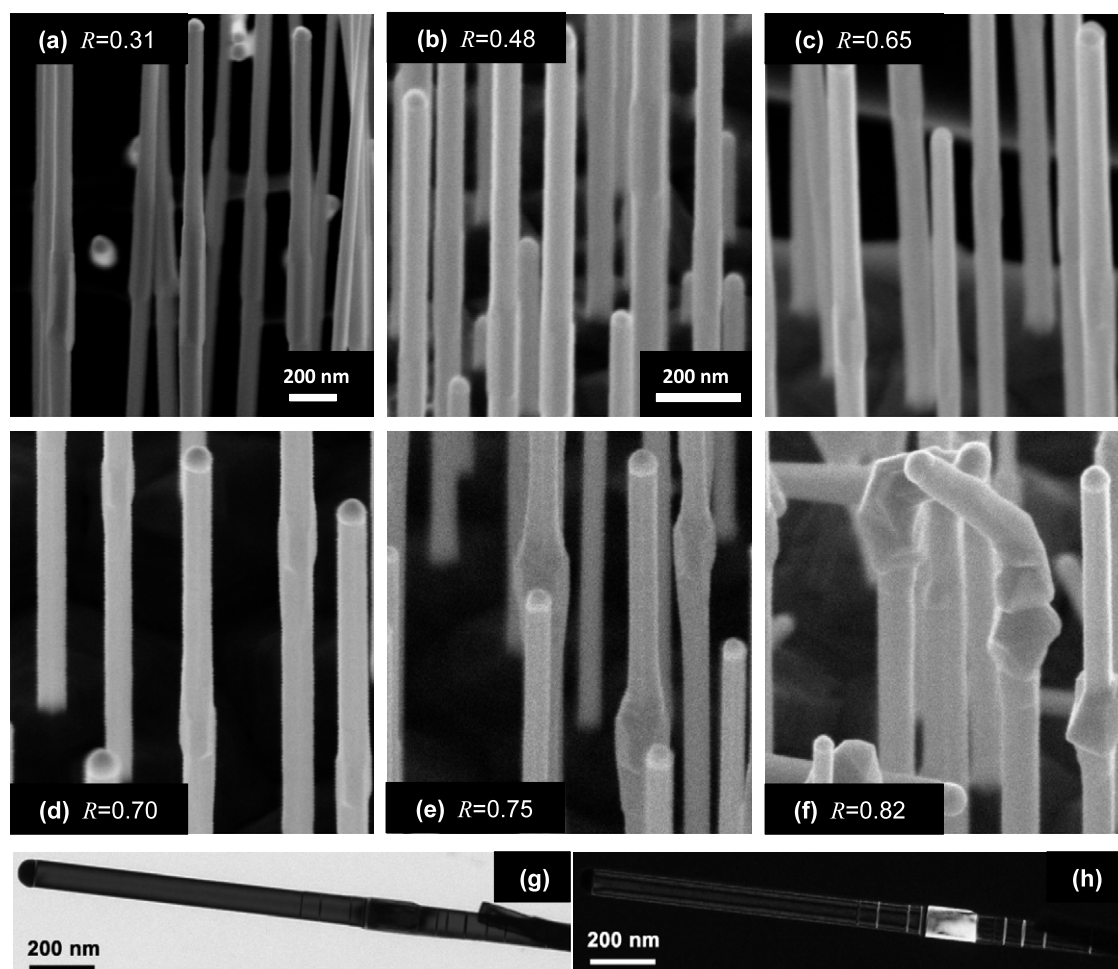
Figure 1. Micrographs of InAs/InAs$_{1-x}$Sb$_x$/InAs double heterostructures with varying TDMASb flux fraction R, indicated in the captions. (a) SEM image—taken at grazing incidence—of the sample grown with the lowest TDMASb flux fraction ($R = 0.31$). (b)–(f) SEM micrographs sharing the scale indicated in (b) and taken at 45° tilt angle; the flux fraction is gradually increasing from $R = 0.48$ in (b) to $R = 0.82$ in (f). (g) Bright field TEM micrograph of a wire grown with $R = 0.70$ (same sample as in (d)). (f) Dark field TEM micrograph of the same NW of (g), obtained by selecting a reflection of the InAsSb ZB diffracted pattern.

of the wires: the quasi-hemispherical In–Au alloy at the tip on the left-hand side, the upper InAs segment with a few, dark contrast, stacking faults, the dark contrast InAs$_{1-x}$Sb$_x$ alloy in the middle, with slightly larger diameter, and the InAs base partially covered by another NW on the right-hand side. An EDX line scan along the NW axis can be found as figure S1 of the supplementary information (available at stacks.iop.org/Nano/23/115606/mmedia), showing that the central segment is indeed Sb rich. The dark field micrograph of figure 1(h) is taken selecting a reflection of the InAs$_{1-x}$Sb$_x$ zincblende (ZB) diffraction pattern, and demonstrates the abruptness of both the upper and lower interfaces between the ZB InAs$_{1-x}$Sb$_x$ and the wurtzite (WZ) InAs segments. A HRTEM image of the central section of the NW with the corresponding fast Fourier transform, clearly identifying the crystal structure of the three segments, is shown in figure S2 of the supplementary information (available at stacks.iop.org/Nano/23/115606/mmedia).

As the TDMASb flux ratio R is increased from 0.75 (figure 1(e)) to 0.82 (figure 1(f)), the morphology of the samples dramatically changes to very disordered NWs. As

one can see in figures 1(a)–(e), the top InAs segments grow along the ⟨111⟩ direction normal to the substrate surface, and no kinks or other defects are visible. On the other hand, in the wires grown at $R = 0.82$ (figure 1(f)), almost no top InAs segment grows in the ⟨111⟩B direction, some InAs segments do not even grow in a 1D fashion, but rather as a complex faceted nanocrystal; in some cases even the InAs$_{1-x}$Sb$_x$ section seems to grow kinked with respect to the InAs base. At higher values of R (not shown) the situation is similar to figure 1(f). For these samples, determination of Sb content in the alloy is very difficult. In fact, an InAs shell grows around the InAsSb segment during the last 30 min of InAs. The shell was observed in the STEM and HRTEM analyses (not shown) and it turned out to be thick enough to significantly alter the Sb composition measurable by EDX. In these samples, due to the presence of the shell, the InAsSb segment is also subject to a significant and very inhomogeneous strain, frustrating the possibility of estimating the content through lattice parameter measurements with electron diffraction.

Although these issues do not presently allow us to precisely determine the threshold Sb concentration for

good quality InAs regrowth, the results show that InAs regrowth over InAsSb alloys is indeed possible, and that a deeper understanding of the $InAs_{1-x}Sb_x$ growth dynamics and structure is necessary. To this aim, we have analyzed $InAs_{1-x}Sb_x$ alloy segments grown on InAs stems, investigating in detail the structural properties of this class of material and their growth dynamics.

Table 1 summarizes the main features of the InAs/$InAs_{1-x}Sb_x$ single heterostructured NWs grown with different TDMASb and TBAs line pressures. Each line summarizes the results from one or more samples grown at the same temperature and with the same line pressure. The second (third) column shows the line pressure P_{TDMASb} (P_{TBAs}) of TDMASb (TBAs) employed during the alloy growth, while R (column four) is the Sb fraction of the total (effective) group V flow in the chamber, as described before for double heterostructures. The Sb content x of the $InAs_{1-x}Sb_x$ alloys estimated with EDX measurements is summarized in column five (x). Unfortunately In and Sb L lines are almost overlapping, making it difficult to estimate very low Sb contents, as in sample A for which we give an upper limit. For all other values, the resolution limits of the technique, confirmed by the statistical spread on the measurements, set an uncertainty of about ± 2 at.% for all compositional measurements. In some cases the Sb concentration has also been determined from TEM diffraction data by measuring the alloy lattice parameter and deriving the x content by assuming the validity of Vergard's law [6]. These estimates have given results very close to those determined by EDX. Furthermore, EDX compositional maps on the wires have always shown homogeneous composition, with no evidence of axial or radial composition changes nor other compositional inhomogeneities in the body of the wires. Antimony incorporation in $InAs_{1-x}Sb_x$ NWs is not a linear function of the flux ratios. As can be seen in table 1, the Sb fraction in the grown NWs (x) is systematically lower than the flux fraction R of the Sb precursor injected in the chamber. This has already been observed in InAsSb alloys [8], and is not surprising since, even in the limiting case of 'pure' InSb, a non-negligible quantity of arsenic is incorporated, as indicated in table 1, and reported in all previous InSb NWs literature, both by CBE [1] and by MOCVD [2]. This is likely to be due to the much easier incorporation of As atoms with respect to Sb atoms in the growing alloy.

The lateral growth (column six) will be discussed later, while *ex situ* In and Au catalyst compositions have been studied by means of EDX measurements which are reported in the last two columns of table 1 as atomic per cent. Here again, all values are affected by a ± 2 at.% uncertainty. The composition of the catalyst is almost always an In–Au alloy with a $\sim$1:2 ratio. In some cases small traces of As and of Sb (<5 at.%) have been found. The 1:2 In:Au ratio is similar to what is generally observed for Au-assisted InAs NWs ($\sim$3:7) [12] and much smaller than the 2:1 ratio typical of InSb [13, 1]. The catalyst composition of sample E (InAs/$InAs_{0.30}Sb_{0.70}$) is richer in indium than the other samples and more similar to the catalyst of InSb NWs. Through the analysis of HRTEM images of the catalyst
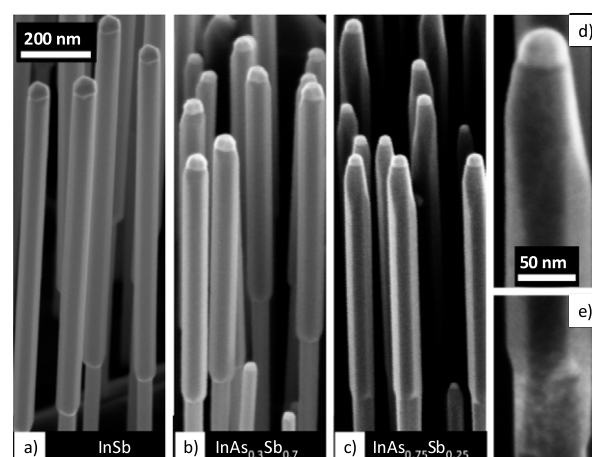
Figure 2. Tilted SEM images of InAs/$InAs_{1-x}Sb_x$ NWs. (a) InAs/InSb NWs ($R = 1$, $x \sim 1$). (b) Sample E ($R = 0.9$, $x \sim 0.70$). (c) Sample C ($R = 0.65$, $x \sim 0.25$). (a)–(c) have the same magnification. (d), (e) are magnified views of the tip and the InAs/InAsSb interface of sample C, showing the details of the faceted morphology, sharing the scale bar indicated in (d).

particles (not shown), on the basis of the d-spacings of the lattice fringes, it has been possible to identify the catalyst alloy in samples A and D to be Au_9In_4.
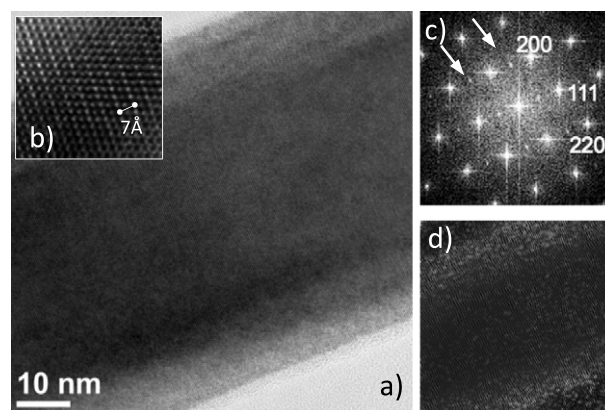
Figure 2 shows SEM micrographs of various NWs taken with the substrate tilted by $60°$ towards the [110] substrate direction. Figure 2(a) is the top part of a InAs/InSb NW sample, while figures 2(b) and (c) are $InAs_{1-x}Sb_x$ NWs with $R = 0.90$ ($x \sim 0.70$) and $R = 0.65$ ($x \sim 0.25$), respectively. InAs/InSb NWs (figure 2(a)), are shown as reference and are characterized in detail in earlier reports, whose main results are [1, 14, 15]: (1) InSb grows with a ZB crystal structure along the $\langle 111 \rangle$ direction perpendicular to the $\{111\}$ surface of the substrate; (2) InSb has six lateral $\{110\}$ facets rotated $30°$ with respect to the InAs ones; (3) *ex situ* catalyst composition after InSb growth is $AuIn_2$, richer in indium with respect to InAs catalyst; (4) InSb diameter is $\sim$20% larger than the InAs stem diameter due to catalyst compositional change between InAs and InSb. As can be seen in figure 2(a), InAs/InSb NWs have the same diameter of the $AuIn_2$ catalyst particle at the tip of the wires. The hexagonal cross section of the InSb segment is evident, and three $\{110\}$ facets are visible, one of which is parallel to the substrate $\{110\}$ cleavage plane. Note that, while at the InAs/InSb interface some other facets are distinguishable [14], at the InSb/catalyst interface there is no evidence of additional faceting. When some arsenic is incorporated into the $InAs_{1-x}Sb_x$ alloy (figure 2(b), $R = 0.90$, $x \sim 0.70$) the morphology remains similar to that of InSb, apart from the fact that the $InAs_{1-x}Sb_x$ lateral size exceeds clearly that of the catalyst particle. The NWs shown in figure 2(c) are made from an As-rich alloy ($R = 0.65$, $x \sim 0.25$). In this case the increased width of the $InAs_{1-x}Sb_x$ segment is even more evident, together with the appearance of clear facets, both at the InAs/$InAs_{1-x}Sb_x$ interface (figure 2(e)), and towards the tip of the wire (figure 2(d)).
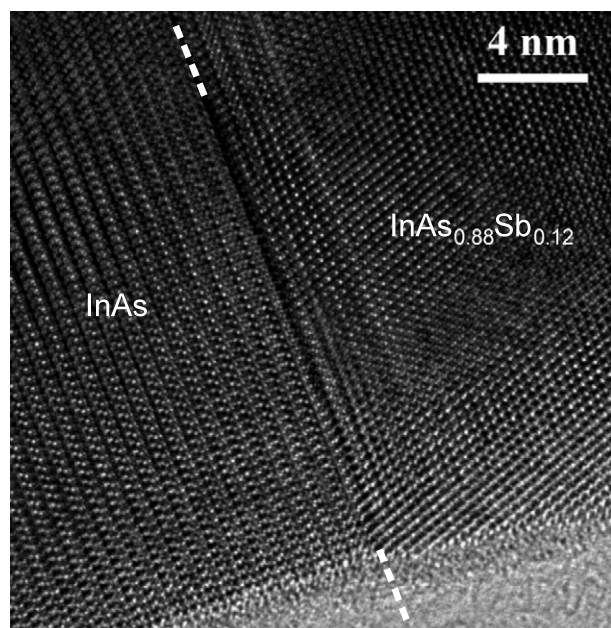
Figure 3. HRTEM image of the InAs/InAs$_{1-x}$Sb$_x$ interface of a NW from sample B (see table 1). The change of contrast at the interface (highlighted by the dashed lines) is due to the change of structure type from WZ, oriented in the [2$\bar{1}\bar{1}$0] zone axis (InAs part at the left), to ZB, oriented in the [110] zone axis (InAs$_{0.88}$Sb$_{0.12}$ part at the right).


Figure 4. (a) HRTEM image taken on the InAs$_{1-x}$Sb$_x$ segment of a NW having $x = 0.12$. (b) Magnified portion of the image (a) where the periodicity of $\sim$7 Å corresponding to the $\frac{1}{2}$\{111\} superstructure spots is visible in the image contrast. A Wiener filter has been applied to the image. (c) FFT taken from the whole image (a). The superstructure spots are indicated by arrows. (d) Inverse FFT generated from (c) by selecting the superstructure spots only.

Single InAs/InAs$_{1-x}$Sb$_x$ heterostructured NWs have been investigated by TEM measurements. HRTEM images show that the InAs bottom segment of the NW has a WZ structure with few stacking faults, as typically found in InAs NWs grown in these conditions. The InAs/InAs$_{1-x}$Sb$_x$ interface is nearly abrupt, with a complete change of contrast from a WZ to a ZB structure after two to three atomic layers (0.7–1.05 nm), as shown in figure 3. The InAs$_{1-x}$Sb$_x$ part has a ZB structure with a regular growth, without twinning or stacking faults. Our results are in agreement with those reported on InAsSb NWs grown by the MOVPE and MBE techniques [8, 28]. All samples observed, regardless of the flux ratio at which they were grown, have interfaces very similar to the one shown in figure 3.

HRTEM images of the InAs$_{1-x}$Sb$_x$ sectors, for compositions richer in As ($R \leq 0.75$, $x \leq 0.50$), show, however, local structural deviations from a normal ZB as described in the following. An HRTEM image taken on a InAs$_{1-x}$Sb$_x$ segment in $\langle 110 \rangle$ orientation, having $x = 0.12$, is shown in figure 4(a). The FFT calculated from the whole image displays $\frac{1}{2}$\{111\} reflections, which are characteristic of a CuPt ordering (figure 4(c)). CuPt ordering in this alloy consists in a peculiar arrangement in which group V layers alternate between As-rich and Sb-rich ones, that can lead to dramatic band structure differences with respect to normal ZB, with effects on structural, optical and electric properties of the alloy [16]. Among the two possible \{111\} ordering directions, the superstructure always arises along the NW growth axis, and has been observed in samples A, B, C, and D, i.e. in all samples with $R \leq 0.75$. In every inspected wire the ordering is never continuous along the entire InAs$_{1-x}$Sb$_x$ segment:

sometimes it can be only detected as weak spots in the FFT, sometimes it is directly visible in the image contrast, as in figure 4(b), where lattice fringes having periodicity $\sim$7 Å can be identified. In those areas where the superstructure is evident, an inverse FFT, generated by selecting the superstructure spots only, demonstrates that the ordered regions are visible only along the NW edges (figure 4(d)). These results are compatible with a superstructure arising only in a laterally overgrown shell, while the core of the InAs$_{1-x}$Sb$_x$ retains the normal ZB structure.

The superstructure $\frac{1}{2}$\{111\} reflections are also visible in diffraction but they are so weak that they can be detected only with a long exposure time or a strong enhancement of the contrast. $\langle 110 \rangle$ selected area electron diffraction patterns taken on the alloy segment of NWs having Sb concentrations $x = 0.25$ and $x = 0.70$ are shown in figures 5(a) and (b), respectively. Both patterns are collected in the $\langle 110 \rangle$ zone axis with the NW growth axis corresponding to the vertical [11$\bar{1}$] direction. An enlarged detail of the pattern of figure 5(a) is displayed in the inset with enhanced contrast. The $\frac{1}{2}$\{111\} superstructure spots are so weak that they are hardly visible. Their weakness confirms that the ordering in the shell of the wires is not continuous. The $\langle 110 \rangle$ diffraction patterns collected on the alloy segment of those NWs that show CuPt order, display also a tripling of the spots at high angle (figure 5(a)). This tripling is always normal to the NW axis. For compositions richer in Sb ($x > 0.5$) the tripling disappears and is replaced by an elongation of the spots in the same direction (figure 5(b)), likely to be correlated to disorder.

Both SEM morphology and TEM results indicate lateral overgrowth in the InAs$_{1-x}$Sb$_x$ segment. The quantification is very difficult due to the lack of an appropriate reference. The only exact reference is the diameter of the InAsSb right below the catalyst particle *during* growth. This is the 'real' diameter before lateral growth takes place. This diameter is different from the InAs stem diameter, as evidenced in InAs/InSb NWs [14], and is related to compositional changes of the
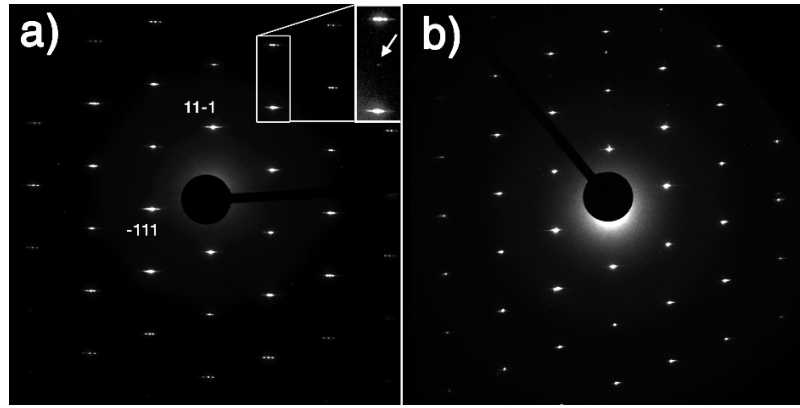
Figure 5. (a) Selected area electron diffraction patterns taken on the alloy segment of a NW from sample C ($R = 0.65$, $x = 0.25$). An enlarged detail of the pattern is displayed in a box at the top right with enhanced contrast to visualize the weak $\frac{1}{2}\{111\}$ superstructure spots (indicated by an arrow). (b) Selected area electron diffraction patterns taken on the alloy part of a NW of sample E ($R = 0.90$, $x = 0.70$). Both patterns are collected in the $\langle 110 \rangle$ zone axis with the NW growth axis corresponding to the vertical [111] direction.

catalyst particle (or changes in the supersaturation condition of the particle) in the presence of Sb. Even knowing the composition of the catalyst particle during growth would be insufficient, since the particle contact angle could depend on the NW and/or the catalyst composition. The 'real' diameter is also different from the *ex situ* after-cooldown catalyst size, which depends also on the details of the cooldown protocol [1].

A reliable way to measure the lateral growth rate consists in growing several samples with different growth times, measuring the NW diameters and extrapolating the zero growth time diameter of the nanowire. Since the Au film dewetting technique yields a wide dispersion of diameters, we have chosen the post-growth particle diameter as a reference with which to compare the samples grown for different times. Hereafter, we will use the term *lateral growth* to indicate $L = \frac{1}{2}(w_{InAsSb} - w_{catalyst})$ where w_{InAsSb} ($w_{catalyst}$) is the width of the InAsSb section (metal catalyst) measured in SEM images. Note that the width of the InAsSb segment can be defined, thanks to the fact that all NWs are very uniform without any sign of tapering at the base of the NWs. For each sample measured, the lateral growth of each wire appears to be independent from its catalyst diameter, at least in the range of catalyst diameters obtained by our dewetting protocol: an example plot of lateral growth versus catalyst diameter is shown in the inset of figure 6, where each point represents the measured value of a single NW.

Figure 6 shows the lateral growth L for various NWs, of different Sb concentrations, and grown for different times. The experimental points (symbols in figure 6) are the values of L obtained by averaging the measurements of more than 30 wires from each sample, on SEM micrographs taken in different, millimeters apart, areas. Error bars represent the standard deviation of the average. Some growths have been repeated to verify reproducibility of the results and the different samples are in excellent agreement with each other. The lines in figure 6 are linear fits of the data. For all three alloy concentrations we find an offset at zero growth time of 10 ± 8, 13 ± 8, and 11 ± 3 nm for Sb content
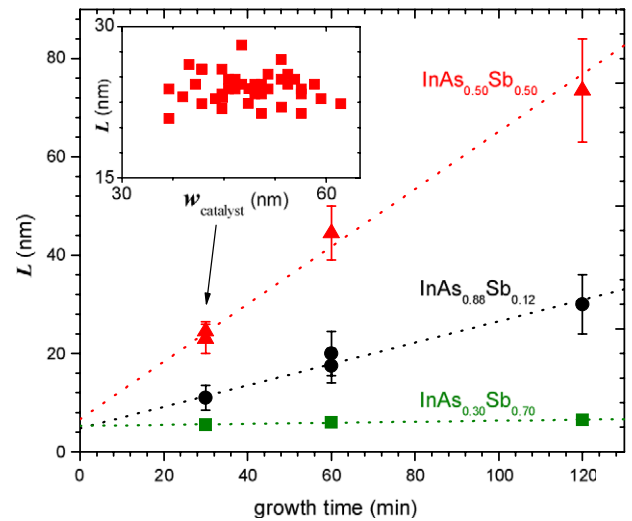

Figure 6. Lateral growth versus growth times of samples B (black disks), D (red triangles) and E (green squares). The dotted lines are the linear fit of the data. The inset is a plot of the lateral growth as a function of catalyst diameter for the individual NWs of the InAsSb 30 min sample indicated by the arrow.

$x = 0.12$, 0.50, and 0.70, respectively. This indicates that the post-growth catalyst width is smaller than the 'real' InAsSb diameter during growth. The sample with highest Sb content ($x = 0.7$) has a lateral growth which is independent of the growth time, with a linear fit slope of 0.01 ± 0.02 nm min^{-1}, i.e. no lateral growth. The lateral growth rates for samples B and D derived from the fitting are reported in column seven of table 1. The lateral growth rates of samples A and C in table 1, for which only the 60 min growth time is available, are calculated as the lateral growth over time ratio and are thus probably overestimated by the approximately constant offset which was observed in samples B, D, and E.

4. Discussion

CuPt ordering has been already observed in two-dimensional (2D) epitaxial growth of InAs$_{1-x}$Sb$_x$ films [17] but never in
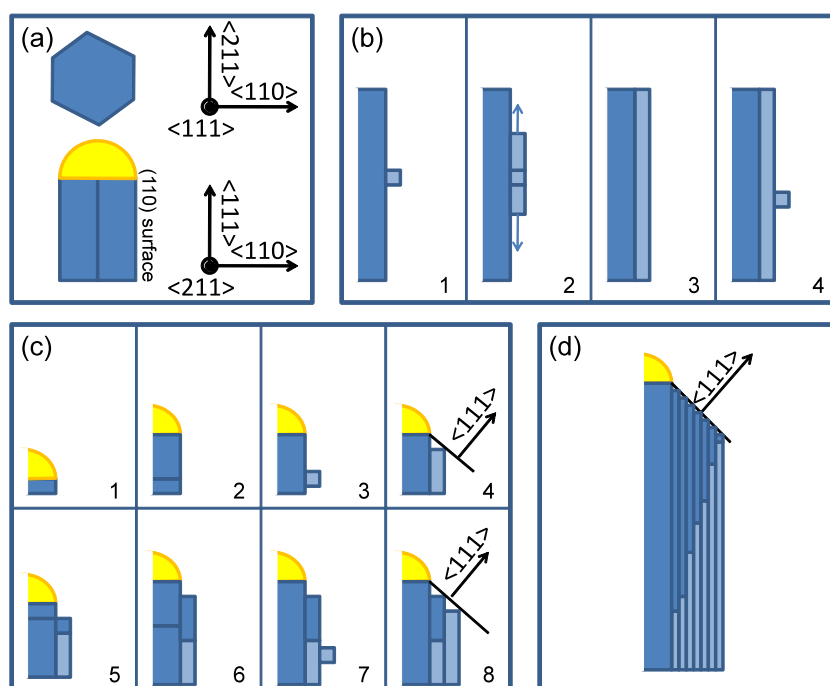
Figure 7. Schematic description of lateral growth process. (a) Top and side view of an InAsSb NW defining the crystallographic orientation of the sketches in the other panels; (b) (110) surface growth by nucleation and step flow; (c) InAsSb NW combined axial and lateral growth (see text); (d) final result.

1D structures. TEM observations in the present work have revealed that this ordering is discontinuous and involves bands of 10–20 nm near the edges of the NWs (figure 4(d)). We have always observed it along the NW axis and never in any of the three {111} reciprocal directions oblique to it. Those directions correspond to {111}*A* faces (terminated by In atoms), which are the not favorable faces for the CuPt ordering in $InAs_{1-x}Sb_x$, as demonstrated by Seong *et al* [18] on $InAs_{1-x}Sb_x$ epitaxial layers. The fact that the ordering does not arise in the sample richest in Sb (sample E) is in agreement with the observation, by Seong *et al*, that during low temperature epitaxial growth of $InAs_{1-x}Sb_x$, after a phase separation of the alloy into alternate layers of different Sb and As content, the order always arises in the As richer part [18, 19]. Although NW and 2D epitaxial growth are completely different in many aspects, the similarities noted here in CuPt ordering are remarkable.

Although already observed in GaSb nanowires [20], the lateral growth mechanism has not been discussed in depth. Lateral sidewalls are generally considered more as areas of transit for diffusing adatoms than incorporation sites [21, 22]. In most cases lateral growth in NWs is considered to be a process taking place at the same time as axial growth, only at a different rate. Thermodynamic and kinetic conditions determine the ratio between the two. For NW growth one attempts, also with the aid of the catalyst metal particle, to enhance the axial growth and to minimize the lateral growth. When the two coexist, one generally obtains 'tapered' nanowires with a NW base that is larger than the tip [23]. This is true, however, only if the lateral growth happens in a layer-by-layer mode. Since the $InAs/InAs_{1-x}Sb_x$

heterostructured NWs are very uniform in size, without any tapering, the lateral growth must take place in a different manner. Our experimental results suggest that lateral growth happens by nucleation and step flow on the lateral {110} facets, in a manner similar to the model of Plante *et al* for GaAs and InAs [24].

This mechanism is schematically described in figure 7. Figure 7(a) explains how the drawings are oriented with respect to InAsSb ZB axes. It is known that the nucleation of new layers on {110} facets is unlikely to occur [25]. However, when a new layer nucleates (see panel 1 of figure 7(b)), it is very rapidly completed to cover the whole (110) facet by a step-flow mechanism (panels 2–3 of figure 7(b)). Then, before the next nucleation event happens (panel 4 of figure 7(b)) a whole layer has been already completed. How this lateral growth is combined with axial growth is described in figure 7(c). Normal InAsSb axial growth, catalyzed by the metal particle, occurs at the particle/InAsSb interface (panels 1–2 of figure 7(c)). If a new layer nucleates at the surface of one of the lateral {110} facets (panel 3 of figure 7(c)) the layer expands by step flow as mentioned above. The step proceeds until encountering a {111} facet at the top or bottom interface, where it is ended, extending the (111) facet itself (panels 3–4 of figure 7(c)). Before the nucleation of a new layer on a side facet, the axial growth proceeds below the particle. As each layer of axial growth is formed, a new step is exposed at the boundary to the top {111}*A* facets that terminate the alloy at the catalyst side. These steps also flow along the facets, letting them advance along with the catalyst, by growing layer after layer following the tip of the wire (panels 5–6 of figure 7(c)), until a new layer nucleates on the sidewalls

7

and the process repeats (panels 7–8 of figure 7(c)). The final result is shown in figure 7(d), where light blue indicates the parts grown by step flow on {110} surfaces, while dark blue is the axial growth together with the layer-by-layer growth of the top {111} facets. The laterally overgrown 'shell' of the alloy is formed in part by step flow of newly nucleated {110} layers, and in part by layer-by-layer growth of the {111}*A* facets around the catalyst. This growth mechanism explains the lateral growth with vertical sidewalls occurring in our InAs/InAs$_{1-x}$Sb$_x$ heterostructured NWs, and is also consistent with the presence of the CuPt superstructure spots in electron diffraction measurements: in fact, studies of the formation of CuPt superstructures in III–V alloys, and in particular in InAsSb alloys, have already been extensively reported for 2D systems [17, 26], and the step-flow mode of growth was assessed to be a necessary condition for its formation [27]. According to our results, for this kind of lateral growth to happen, the simultaneous presence of large amounts of Sb and As seem to be necessary. In fact, in the samples with low Sb content (A, and B in table 1) the lateral growth is very limited, although the CuPt superstructure has been observed. In these samples the Sb concentration is $x \leq 0.12$, and the TDAMSb flux ratio is $R \leq 0.48$. At the other extreme, the E and InSb samples (with $x \geq 0.70$ and $R \geq 0.90$) have no measurable lateral growth, nor any sign of CuPt ordering. The two samples with intermediate composition, C ($x = 0.25$, $R = 0.65$) and D ($x = 0.5$, $R = 0.75$), have the fastest lateral growth, greater than 5 Å min^{-1}. Thus the simultaneous presence of As and Sb atoms at the surface of the side facets seems to increase the nucleation probability of a new layer.

5. Conclusions

We have investigated the growth of InAs/InAs$_{1-x}$Sb$_x$ heterostructured NWs in a wide range of Sb compositions. The main findings are that the alloys, in the Sb compositional range explored, have always the zincblende crystal structure, and that there is lateral growth along with the axial growth, occurring in a nucleation and step-flow mode. The lateral growth rate depends on the As:Sb ratio, being maximum around the 1:1 value. The lateral overgrown part, observed by TEM, displays regions of CuPt ordering, never observed before in semiconductor nanowires. The CuPt ordering is likely to be related to the step-flow growth of the sidewalls. Additionally, we have shown that for an Sb content up to an intermediate value it is possible to grow good quality InAs/InAs$_{1-x}$Sb$_x$/InAs double heterostructured NWs. This offers a new degree of freedom in device engineering, taking advantage of the outstanding properties of both InAs and antimonide-based compounds.

Acknowledgments

References

[1] Ercolani D, Rossi F, Li A, Roddaro S, Grillo V, Salviati G, Beltram F and Sorba L 2009 InAs/InSb nanowire heterostructures grown by chemical beam epitaxy *Nanotechnology* **20** 505605

[2] Caroff P, Messing M E, Borg B M, Dick K A, Deppert K and Wernersson L-E 2009 Insb heterostructure nanowires: Movpe growth under extreme lattice mismatch *Nanotechnology* **20** 495606

[3] Ashley T, Dean A B, Elliott C T, Pryce G J, Johnson A D and Willis H 1995 Uncooled high-speed InSb field-effect transistors *Appl. Phys. Lett.* **66** 481

[4] Nilsson H A, Caroff P, Thelander C, Larsson M, Wagner J B, Wernersson L-E, Samuelson L and Xu H Q 2009 Giant, level-dependent g factors in InSb nanowire quantum dots *Nano Lett.* **9** 3151

[5] Roddaro S, Pescaglini A, Ercolani D, Sorba L, Giazotto F and Beltram F 2010 Hot-electron effects in InAs nanowire josephson junctions *Nano Res.* **4** 259

[6] Vurgaftman I, Meyer J R and Ram-Mohan L R 2001 Band parameters for III–V compound semiconductors and their alloys *J. Appl. Phys.* **89** 5815

[7] Pitanti A, Ercolani D, Sorba L, Roddaro S, Beltram F, Nasi L, Salviati G and Tredicucci A 2011 InAs/InP/InSb nanowires as low capacitance n–n heterojunction diodes *Phys. Rev. X* **1** 011006

[8] Borg B M, Dick K A, Eymery J and Wernersson L-E 2011 Enhanced Sb incorporation in InAsSb nanowires grown by metalorganic vapor phase epitaxy *Appl. Phys. Lett.* **98** 113104

[9] Plissard S, Dick K A, Wallart X and Caroff P 2010 Gold-free GaAs/GaAsSb heterostructure nanowires grown on silicon *Appl. Phys. Lett.* **96** 121901

[10] Dheeraj D L, Patriarche G, Largeau L, Zhou H L, van Helvoort A T J, Glas F, Harmand J C, Fimland B O and Weman H 2008 Zinc blende GaAsSb nanowires grown by molecular beam epitaxy *Nanotechnology* **19** 275605

[11] Jensen L E, Björk M T, Jeppesen S, Persson A I, Ohlsson B J and Samuelson L 2004 Role of surface diffusion in chemical beam epitaxy of InAs nanowires *Nano Lett.* **4** 1961

[12] Fröberg L E, Wacaser B A, Wagner J B, Jeppesen S, Ohlsson B J, Deppert K and Samuelson L 2008 Transients in the formation of nanowire heterostructures *Nano Lett.* **8** 3815

[13] Caroff P, Wagner J B, Dick K A, Jeppsson M, Nilsson H A, Deppert K, Samuelson L, Wallenberg L R and Wernersson L E 2008 High-quality InAs/InSb nanowire heterostructures grown by metal-organic vapor-phase epitaxy *Small* **4** 878

[14] Lugani L, Ercolani D, Rossi F, Salviati G, Beltram F and Sorba L 2010 Faceting of InAs-InSb heterostructured nanowires *Cryst. Growth Des.* **10** 4038

[15] Lugani L, Ercolani D, Beltram F and Sorba L 2011 Growth mechanism of InAs/InSb heterostructured nanowires grown by chemical beam epitaxy *J. Cryst. Growth* **323** 304

[16] Wei S-H and Zunger A 1997 Fingerprints of cupt ordering in iii-v semiconductor alloys: valence-band splittings, band-gap reduction, and x-ray structure factors *Phys. Rev. B* **57** 8983

[17] Jen H R, Ma K Y and Stringfellow G B 1989 Long-range ordering in InAsSb *Appl. Phys. Lett.* **54** 1154

[18] Seong T-Y, Norman A G, Ferguson I T and Brooker G R 1993 Transmission electron microscopy and transmission electron diffraction structural studies of heteroepitaxial $InAs_{1-y}Sb_y$ molecular-beam epitaxial layers *J. Appl. Phys.* **73** 8227

[19] Seong T-Y, Booker G R, Norman A G and Ferguson I T 1994 Atomic ordering in molecular beam epitaxial InAsySb1y natural strained layer superlattices and homogeneous layers *Appl. Phys. Lett.* **64** 3593

[20] Jeppsson M, Dick K A, Wagner J B, Caroff P, Deppert K, Samuelson L and Wernersson L-E 2008 GaAs/GaSb nanowire heterostructures grown by movpe *J. Cryst. Growth* **310** 4115

[21] Dubrovskii V G *et al* 2009 Role of nonlinear effects in nanowire growth and crystal phase *Phys. Rev.* B **80** 205305

[22] Dubrovskii V G *et al* 2009 Gibbs–Thomson and diffusion-induced contributions to the growth rate of Si, InP, and GaAs nanowires *Phys. Rev.* B **79** 205316

[23] Chen C, Plante M C, Fradin C and LaPierre R R 2006 Layer-by-layer and step-flow growth mechanisms in GaAsP/GaP nanowire heterostructures *J. Mater. Res.* **21** 2801

[24] Plante M C and LaPierre R R 2009 Analytical description of the metal-assisted growth of iiiv nanowires: axial and radial growths *J. Appl. Phys.* **105** 114304

[25] Faustjr J and John H 1962 Growth facets on III–V intermetallic compounds *J. Phys. Chem. Solids* **23** 1119

[26] Ihm Y-E and Otsika N 1987 Ordering in GaAsSb grown by molecular beam epitaxy *Appl. Phys. Lett.* **51** 2013

[27] Stringfellow G B and Chen G S 1991 Atomic ordering in iii/v semiconductor alloys *J. Vac. Sci. Technol.* **9** 2182

[28] Xu T *et al* 2012 Faceting, composition and crystal phase evolution in III–V antimonide nanowire heterostructures revealed by combining microscopy techniques *Nanotechnology* **23** 095702